Numerical Simulation Study on the Dynamics of Bluff-Body Flames under Oxygen-Lean Conditions

Fuquan Deng [1,2], Minwei Zhao [1], Shunchuang Qin [1], Zhaokun Wang [2], Yongliang Xie [3], Hongtao Zheng [1], Xiao Liu [1,*] and Feng Zhang [4,*]

1   College of Power and Energy Engineering, Harbin Engineering University, Harbin 150001, China;
    adsdengfuquan@hrbeu.edu.cn (F.D.); zhaominwei@hrbeu.edu.cn (M.Z.)
2   Department of Mechanical Engineering, The Hong Kong Polytechnic University,
    Hong Kong SAR 999077, China
3   School of Mechanical Engineering, Southwest Jiaotong University, Chengdu 610031, China
4   College of Mechanical and Vehicle Engineering, Hunan University, Changsha 410082, China
*   Correspondence: liuxiao_heu@163.com (X.L.); fengzhang@hnu.edu.cn (F.Z.)

Abstract: As modern aeroengine combustors advance towards high temperatures, afterburners are inevitably affected by diminished oxygen content in incoming flows, thus affecting combustion efficiency, instability, and flammability limits. In this study, the dynamic combustion characteristics of V-shaped bluff body-stabilised diffusion flames were investigated using a large eddy simulation method with an oxygen mass fraction range of 14–23% and temperatures ranging from 900 to 1100 K. The results show the significant effects of oxygen content and inflow temperature on the flame/flow behaviours downstream of the bluff-body flame holder. In a separated shear layer, two distinct modes of flow/flame shedding are observed when varying the oxygen content and inflow temperature. The results show that BVK instability governs the far-field wake flow/flame features, whereas the oxygen concentration and temperature significantly affect their oscillation amplitudes. In addition, variations in the incoming oxygen content and temperature shift the axial position of the transition from KH instability to BVK instability. Finally, a spectral analysis is conducted to investigate the characteristics of pressure and heat release pulsations under different scenarios. This study highlights the importance of oxygen content on the combustion dynamics of bluff body-stabilised diffusion flames at various temperatures, which is essential for optimising combustion efficiency and stability in practical applications.

Keywords: oxygen content; bluff-body diffusion flame; vortex shedding; dynamic combustion characteristic; large eddy simulation

1. Introduction

As current aeroengine technology advances towards higher temperatures [1–3], heat capacity, and efficiency [4,5], the oxygen content in the incoming flow of the afterburner is reduced significantly. The decline in oxygen content significantly affects the combustion reaction rate and flame propagation speed, thus resulting in significant changes in the combustion dynamics, including vortex–flame interactions, vortex-shedding patterns, flame morphology, exothermicity, and pressure pulsations, which significantly affect the combustion efficiency, flame stability, and burn flammability limits [6–9]. The fundamental causes of combustion dynamics are complex phenomena encompassing various aspects, including the flow field structure [10], vortex motion [11], fuel injection [12], atomisation [13], evaporation, turbulent mixing [14], and chemical reactions [15]. Therefore, the effect of oxygen content on the combustion dynamics of bluff body-stabilised diffusion flames must be investigated.

Researchers have emphasised the substantial effect of oxygen ratio on flame behaviour. Liu et al. [16] performed numerical simulations to investigate the flame characteristics and

effects of a bluff body under low oxygen ratios. They discovered that, as the oxygen content decreased, the flame reaction zone exhibited relatively weaker reactivity, accompanied by lower temperatures and OH concentrations. Additionally, the results showed a significant distribution of CH_2O (formaldehyde) under low-oxygen conditions, thus indicating partial premixing and pre-ignition reactions within the flame recirculation zone. Roy et al. [17] numerically investigated the effects of adding diluents (CO_2 and H_2O) to bluff-body flames. The results showed as the oxygen content decreased, the temperature of the bluff-body flame decreased, whereas higher diluent concentrations and fuel velocities diminished the flame. Wang et al. [18] numerically investigated the effect of the oxygen content on the combustion characteristics of premixed methane bluff-body flames. They discovered that the bluff-body flames formed by low-oxygen combustion were far downstream of the nozzle, exhibited a low laminar flame speed, and yielded minimal NOx. Kumar et al. [19] and Mishra et al. [20] investigated the effect of adding N_2 on a coaxial liquefied petroleum gas jet diffusion bluff-body flame. This study showed that the length of the bluff-body flames increased with the addition of N_2, whereas the soot-free length fraction increased with the addition of N_2 under a reduced flame temperature. Hosseini et al. [21] and Noor et al. [22] investigated the effect of oxygen content on the characteristics of bluff-body flameless combustion. The results showed that when the oxygen content decreased, the maximum temperature decreased, and the temperature distribution in the combustor remained relatively uniform. Additionally, studies have shown that the incoming temperature significantly affects the dynamic characteristics of bluff-body flames [23,24]. Shanbhogue et al. [25] discovered that an increase in temperature increased the gas expansion ratio, which affected both the vorticity sources and sink terms. Consequently, the baroclinic vorticity changed, thus increasing the flow dilatation and gas kinematic viscosity. Emerson et al. [26] experimentally investigated the dynamic combustion characteristics of bluff-body premixed flames at high Reynolds numbers. Their findings demonstrated that variations in the temperature changed the density ratio of the flame surface. The length of the recirculation zone and the peak reverse velocity increased with the density ratio. Conversely, a decrease in the density ratio increased the asymmetry and coherence between the flame branches, thereby indicating the formation of large structures in the wake. Emerson et al. [27] experimentally investigated the wake and flame characteristics of bluff-body flames and discovered that the density ratio significantly affected the flow field characteristics and flame sheet dynamics. Specifically, as the density ratio decreased, the correlation and asymmetric motion inside the flame increased. Erickson [23,24] numerically investigated the effect of temperature on the stability of bluff-body premixed flames and discovered that an increase in temperature increased the amplitude of fluid dynamics, thus resulting in a transition from broadband to tonal behaviour. This shift occurred because the increase in temperature decreased the flame temperature ratio, thereby reducing the combustion exothermicity. In addition, higher temperatures increased the flame velocity, thus causing the flame to flow away from the bluff-body wake. Moreover, when the temperature ratio increased, the dominance of the asymmetric Von Karman mode decreased.

Currently, experimental and numerical simulations studies that investigate the effects of temperature and oxygen content on dynamic combustion characteristics are insufficient. Specifically, the effect of oxygen content on the characteristics of dynamic combustion remains unclear. Therefore, the effect of oxygen content at different temperatures on the dynamic combustion characteristics of bluff-body non-premixed flames must be investigated to provide theoretical guidance for improving the combustion efficiency and suppressing unstable combustion.

2. Numerical Method Computational and Mathematical Model

2.1. Numerical Method

Large eddy simulation (LES) uses subgrid-scale (SGS) turbulence models to directly solve large-scale vortex clusters and represent small-scale vortex structures. The SGS stress term [28] is used in the LES to reflect the effect of filtered small-scale vortices on the flow

field. In this study, the algebraic wall-modelled LES model was utilised for numerical simulation as it can significantly minimise the requirements for the wall mesh scale. The compressible Reynolds-Averaged Navier-Stokes (RANS) solution mode was used for the boundary layer near the wall to avoid turbulence structures with extremely small analytical scales in the area near the wall and to reduce the amount of computation. The fuel utilised in the combustor in this study was liquid fuel. Mass, momentum, energy, and component transfers between phases must be incorporated throughout the numerical simulation. The force distribution, motion trajectory, heating, cooling, and evaporation boiling of the fuel droplets were simulated using a discrete phase model. To simulate turbulent combustion in the bluff body, a partly premixed combustion model was used in this study. The mixing fraction *f* and process variable *C* were introduced as independent variables for the laminar functionally graded materials (FGM) form in the FGM combustion calculation model [29]. The distribution of the process variables was obtained by solving their transport equations; subsequently, the FGM form data were read to obtain the distribution patterns of the temperature and component mass fraction.

In this study, the reaction mechanism of $C_{12}H_{23}$ proposed by Kundu et al. [30] (13 species and 15 reactions) was used to substitute the jet fuel component in the numerical modelling of a model combustor to compute the combustion reaction, as shown in Table 1.

Table 1. $C_{12}H_{23}$ simplified reaction mechanism [30].

No.	Reactions	A	n	Ea
1	$C_{12}H_{23} + N_2 =>12CH + 11H + N_2$ FORD/$C_{12}H_{23}$ 0.8/ FORD/N_2 0.8/	5.50×10^{10}	0.00	3.00×10^4
2	$N_2 + CO + HO_2 =>CO_2 + OH + N_2$ FORD/N_2 0.1/ FORD/CO 1.0/ FORD/HO_2 1.0/	3.50×10^{13}	0.00	2.29×10^4
3	$H_2 + 2O =>O_2 + H_2$ FORD/H_2 1.0/ FORD/O 2.0/	1.00×10^{18}	0.00	0.00
4	$H_2 + OH<=>H_2O + H$	1.17×10^{11}	1.30	3.62×10^3
5	$H_2 + O<=>H + OH$	2.50×10^{15}	0.00	6.00×10^3
6	$H + O_2<=>O + OH$	4.00×10^{14}	0.00	1.80×10^4
7	$H_2 + 2H<=>2H_2$	4.00×10^{20}	−1.00	0.00
8	$H + O_2<=>HO_2$	1.00×10^{15}	−0.87	0.00
9	$H + HO_2<=>H_2 + O_2$	1.50×10^{14}	0.00	0.00
10	$O + HO_2<=>OH + O_2$	2.50×10^{13}	0.00	0.00
11	$CO + OH<=>CO_2 + H$	1.51×10^7	1.30	-7.58×10^2
12	$2CH + N_2<=>C_2H_2 + N_2$	1.00×10^{18}	0.00	-7.58×10^2
13	$C_2H_2 + O_2<=>2CO + H_2$	3.00×10^{16}	0.00	1.90×10^2
14	$CH + O<=>CO + H$	1.00×10^{12}	0.70	0.00
15	$CH + OH<=>CO + H_2$	1.00×10^{13}	0.00	0.00

2.2. Numerical Configuration and Simulated Case

2.2.1. Model Structure

The combustion model developed by Roach et al. [31] was used to perform calculations, Because of the symmetry of the combustion model, one-third of the spanwise width was used in the numerical calculations, which resulted in a calculation domain size of 1150 mm × 100 mm × 50 mm. The flame stabiliser in the afterburner featured a conventional V-shaped bluff-body structure with a 30° top angle and a trailing edge groove width of D = 40 mm, as shown in Figure 1.

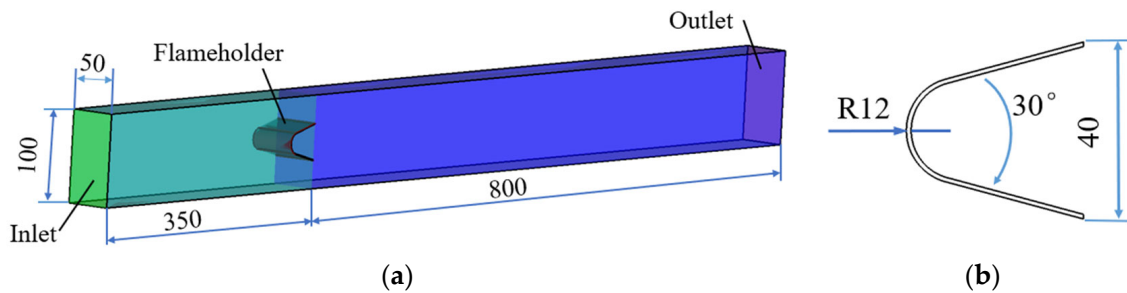**Figure 1.** Schematic diagram of bluff-body combustor (units: mm). (**a**) Combustor, (**b**) Bluff body.

2.2.2. Meshing

On both sides of the combustor, periodic boundary conditions were imposed to densify the mesh locally at the bluff body and recirculation zone. The minimum mesh size of the bluff-body surface in the normal direction was 0.2 mm. In the simulation, y+ < 10 was adequate to fulfil the requirements of the wall function under the settings used in this study. Additionally, 10 densified layers were implemented, as shown in Figure 2.
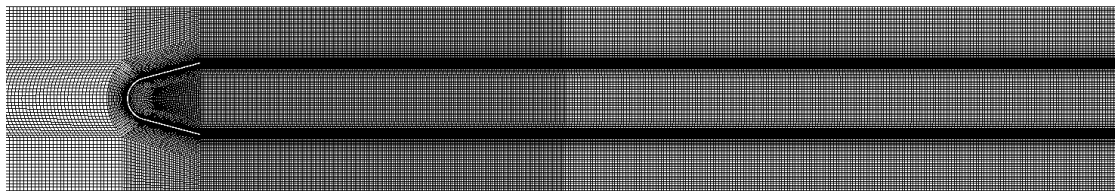

Figure 2. Schematic diagram of grid used.

The mesh independence in unsteady numerical simulations was verified under a Mach number of 0.2, temperature of 900 K, and pressure of 0.1 MPa. The velocity time series of the core position of the backflow zone behind the bluff body and the points at the shear layer were tested during the calculation process, and a spectral analysis was performed. The slope of the red line in Figure 3 was $-5/3$, and the spectral curve reflected Kolmogorov's $-5/3$ power law, thus demonstrating that the mesh size satisfied the basic LES calculation conditions [32]. Consequently, for both stable and unsteady calculations, a mesh with 3.4 million nodes was selected in this study.
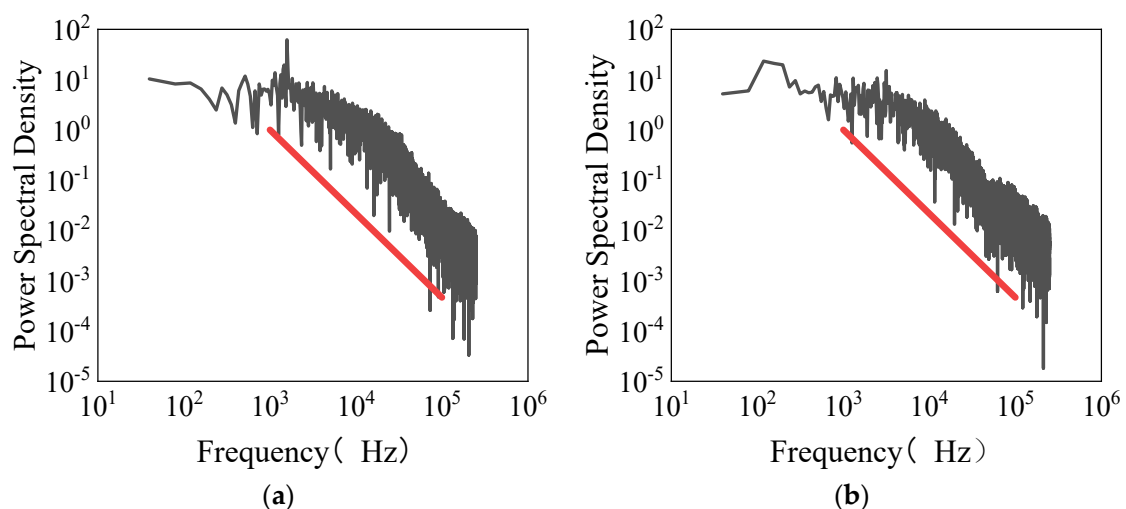

Figure 3. Verification of mesh independence in unsteady numerical simulations. (**a**) Shearing layer position, (**b**) Core location of the recirculation zone.

2.2.3. Computational Domain and Boundary Conditions

Fluent was used to perform numerical simulations on a bluff-body model combustor. Control variables were utilised in this study to investigate the effect of oxygen content (mass fraction) on the bluff-body performance at various inlet temperatures. The oxygen excess ratio is 1.25 at 23% oxygen, 0.96 at 20% oxygen, 0.67 at 17% oxygen and 0.37 at 14% oxygen. The operating conditions are shown in Table 2.

Table 2. Operating conditions to investigate effect of oxygen content on the combustion performance of the bluff body.

	Pressure/MPa	Temperature/K	Mach Number	Oil-to-Gas Ratio	Oxygen Content/%
Case1	0.1	900	0.2	0.03	14–23
Case2	0.1	1000	0.2	0.03	14–23
Case3	0.1	1100	0.2	0.03	14–23

2.3. Model Verification

To test the accuracy of the model, non-reactive and reactive numerical simulations were carried out under the experimental conditions described in [33]. The model was validated using the following boundary conditions: inlet air velocity, 17.3 m/s; temperature, 288 K; pressure, atmospheric pressure; and equivalent ratio, 0.65. Figure 4 shows a comparison of the calculated results with the experimental data at different axial positions, which shows good agreement between the two sets of data.
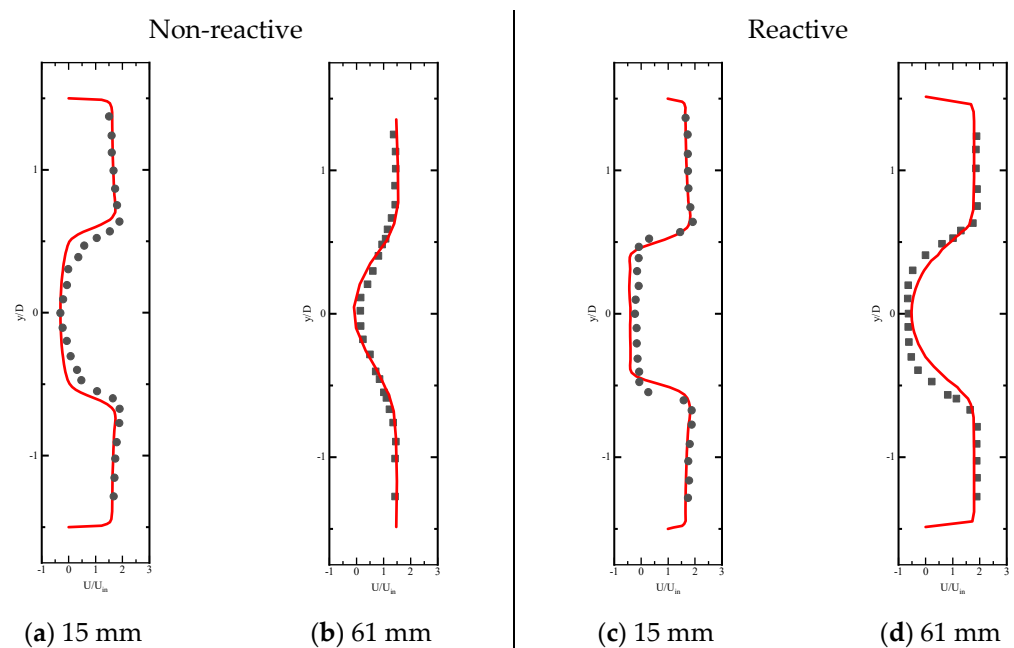

Non-reactive   Reactive

(**a**) 15 mm   (**b**) 61 mm   (**c**) 15 mm   (**d**) 61 mm

Figure 4. Normalized axial velocity of non-reactive and reactive flow at 15 mm and 61 mm positions behind the bluff body. Points: experimental data; solid lines: numerical simulation results.

3. Results and Discussion

3.1. Effect of Oxygen Content on Dynamic Combustion Characteristics under Various Temperatures

The vortex structure and flame morphology were investigated under the following conditions: oxygen content, 23–14%; inflow temperature range, 900–1100 K; Ma = 0.2; and operating pressure p = 0.1 MPa.

3.1.1. Vortex Structure

The Q-criterion, as represented by velocity, was used to identify the vortex structures [25]. As shown in Figure 5, the effect of oxygen content on the vortex structure

during the moment of maximum amplitude of pressure pulsation is illustrated based on a non-dimensional Q-criterion isosurface with a Q value of 5×10^7 s^{-1} under varied inflow temperatures. Generally, as illustrated in Figure 5, both the oxygen content and inflow temperature significantly affect the vortex shedding modes, flame–vortex interactions, vortex structure, and the magnitude of the vortex formed downstream of the V-gutter flame holder in both the separated shear layer and wake.
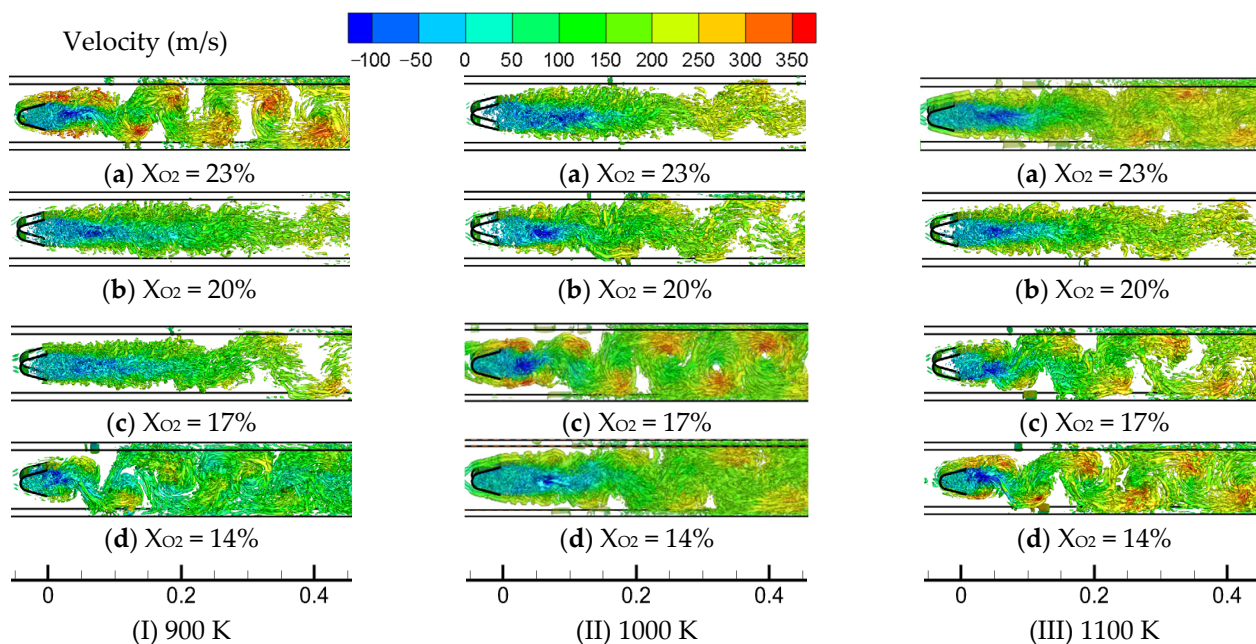

Figure 5. Effect of oxygen content on vortex structure shedding behind the V-shaped bluff body at various temperatures.

At T = 900 K, Bénard-von Kármán (BVK) instability dominated the flow within the entire reactive flow behind the V-shaped bluff body at X_{O2} = 23%, where substantial oscillations were exhibited in both the shear layer and wake. As the oxygen content decreased from 23% to 20%, the vortices in the reacting flow were reduced and propagated symmetrically downstream in an almost up–down manner, which signified Kelvin–Helmholtz (KH) instability. Further reducing the oxygen content to 17% did not affect KH instability within the separated shear layer, whereas BVK instability emerged approximately 200 mm downstream from the trailing edge of the bluff body. At X_{O2} = 14%, the overall flow in the near region behind the V-shaped gutter flame holder transitioned from KH instability to BVK instability and exhibited clear sinuous and undulating BVK instability characteristics.

At T = 1000 K and X_{O2} = 23%, the flow structure within the separated shear layer was characterised by KH instability, whereas it exhibited mild BVK instability oscillations approximately 280 mm downstream from the bluff body. The number of vortices in the cavity of the V-shaped bluff body decreased significantly, and the vortex tubes within the region near the V-shaped bluff body exhibited an approximately linear symmetrical distribution. This might be attributed to the competition between the expansion of the vortex volume caused by exothermic combustion and the oblique/viscous pressure vortex generated by the bluff body, which ultimately yielded a smaller average vortex volume and scale. As the oxygen content decreased from 23% to 14%, the BVK instability in the reacting flow intensified, thus resulting in an increase in the oscillation amplitude; moreover, the location at which the initiated BVK instability shifted gradually upstream. At an oxygen content of 14%, both the entire shear layer and wake flow exhibited a high degree of oscillating BVK instability.

KH instability was evident in the near-field flow behind the V-shaped gutter flame holder at an incoming temperature of 1100 K and oxygen concentration of 23%, whereas

BVK instability emerged approximately 180 mm downstream from the trailing edge of the bluff body. As the oxygen content was reduced to 20%, the BVK instability weakened, thus resulting in a significant reduction in the oscillation amplitude, and the location where the reacting flow translated from KH instability to BVK instability shifted downstream. The overall reaction flow indicated KH instability. By further reducing the oxygen content, the intensity of the vortices within the reacting flow increased, thus resulting in the predominance of large-scale BVK oscillations within both the shear layer and wake. Furthermore, as the oxygen content decreased from 17% to 14%, the magnitude of the oscillations in the reacting flow increased significantly.

3.1.2. Flame Structure

Figures 6 and 7 illustrate the effect of oxygen content on the OH concentration and temperature fields, respectively, at various inflow temperatures. Clearly, the flame structures characterised by both the OH concentration and temperature were highly similar to the flow field features.
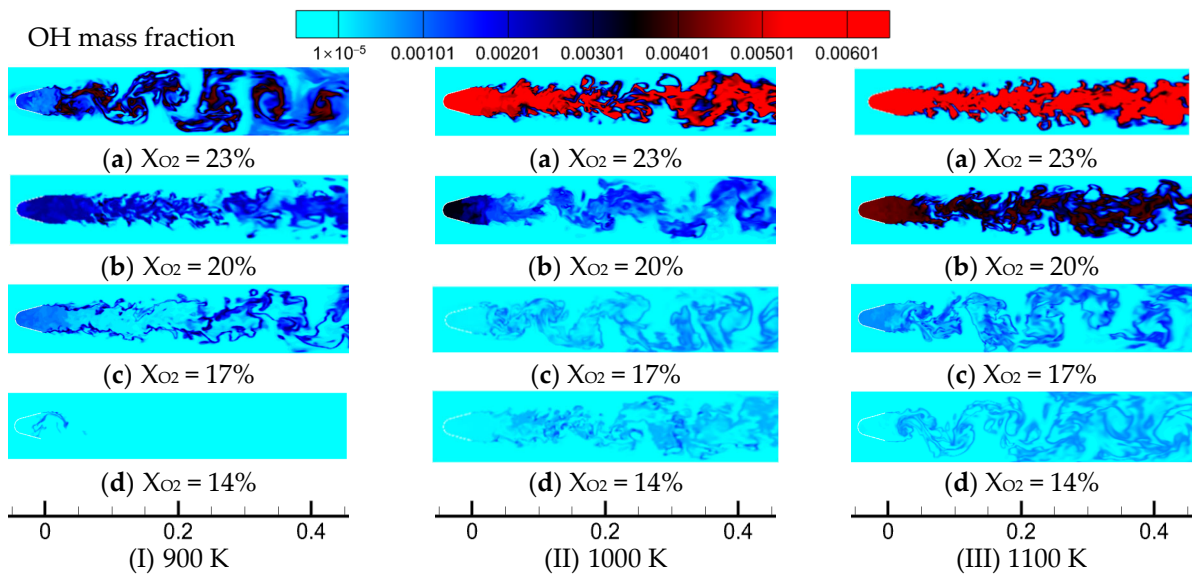

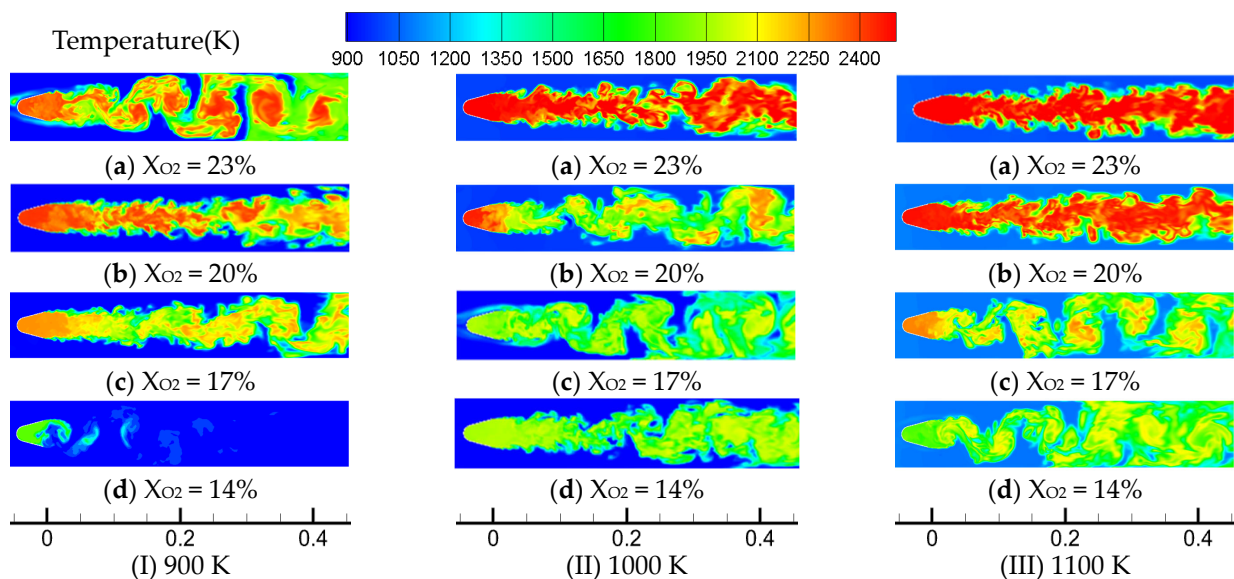**Figure 6.** Effect of oxygen content on the OH concentration field at various temperatures.

Figure 7. Effect of oxygen content on the temperature field at various temperatures.

At T = 900 K and X_{O2} = 23%, the relationship between the flow and combustion resulted in the formation of a substantial large-scale vortex roll-up, which generated a vigorous vorticity that surrounded and entrained the flame. Consequently, the flame front was almost parallel to the vortex structure within the reactive flow, thus exhibiting a distinctive sinuous BVK instability. Excessive shear stress within the vortex may extinguish the enclosed flame. Subsequently, as the shear stress decreases, the unburned high-temperature combustible mixture surrounded by the vortex shedding may be reignited, which can potentially induce intense exothermic pulsations. When the oxygen content was reduced to 20%, the flame structure exhibited KH instability, which was extremely similar to the characteristics of the vortex structure. In addition, both the OH concentration and temperature decreased, thus indicating weakened combustion intensity. Moreover, the OH concentration was distributed continuously along the streamwise direction and dominated both the upper and lower shear layers, as well as the central flow field. As the oxygen content continued to decrease to 17%, the combustion intensity decreased further. Although the OH concentration distribution was continuous along the streamwise direction, it was primarily confined to the upper and lower shear layers, with minimal presence in the central reacting flow field. When the oxygen content was reduced to 14%, the flame approached complete extinguishment.

At T = 1000 K and X_{O2} = 23%, the OH concentration and temperature demonstrated a symmetric distribution of KH instability in the near field, whereas it presented slight oscillations corresponding to BVK instability in the far wake. At the location where KH instability transitioned to BVK instability, the flame disintegrated into smaller fragments. When the oxygen content was reduced from 23% to 14%, the combustion intensity decreased progressively, thus resulting in a gradual reduction in both the OH concentration and temperature. Throughout the reaction flow, the flame front exhibited a significant S-shaped oscillation. In particular, at X_{O2} = 20%, the OH radicals extended across both the upper and lower shear layers as well as in the central reacting flow field, thus resulting in the presence of localised high-temperature regions with elevated OH concentrations. As the oxygen content decreased further, the OH radicals were limited to the upper and lower shear layers and showed a more uniform temperature distribution across the entire reacting flow.

At T = 1100 K, the combustion intensity of the reacting flow increased with the oxygen content and was accompanied by an increase in the OH concentration and temperature. When $X_{O2} \geq 20\%$, OH radicals appeared throughout the reacting flow, and the flame disintegrated into smaller fragments at locations with strong local shear forces. However, when $X_{O2} \leq 17\%$, the combustion intensity decreased significantly. Additionally, when the OH concentration in the central region of the reacting flow was extremely low, the flame approached extinguishment inside the region and presented strong shear forces before reigniting immediately.

3.2. Effect of Oxygen Content on Instantaneous Reaction-Flow Field

To further investigate the effect of oxygen content on the dynamic combustion characteristics within the bluff body, we investigated the effect of oxygen content on the instantaneous reaction flow field, including the evolution of the flow field and flame morphology under *Ma* = 0.2, *T* = 900 K, and *p* = 0.1 MPa.

The flow structure behind the V-shaped gutter flame holder significantly affected the dynamic combustion characteristics, such as the flame morphology, exothermic pulsation, and pressure pulsation. Figure 8 shows the temporal evolution of the streamline behind the V-shaped gutter flame holder at X_{O2} = 23%. The presence of a low-pressure region behind the flame holder resulted in the generation of numerous small-scale vortices, which propagated downstream and progressively developed and merged, before eventually coalescing to form large-scale vortices near the trailing edge of the bluff body. Under the effect of shear forces, large-scale vortices eventually segregated and detached from the shear layer. Consequently, asymmetric and alternating von Karman vortex shedding occurred in the near-wake region, thus resulting in the formation of two asymmetric vortices

rotating in opposite directions, which closely resembled BVK instability. Furthermore, the pressure inside the vortex was considerably lower than the external pressure. The vortex propagated intermittently and periodically downstream, thus resulting in periodic fluctuations in pressure in the near-wake region. As shown in Figure 8, the vortex-shedding process from (a) to (f) formed a complete shedding cycle. The estimated vortex-shedding period was approximately 7×10^{-4} s, which corresponded to a shedding frequency of approximately 1428 Hz.
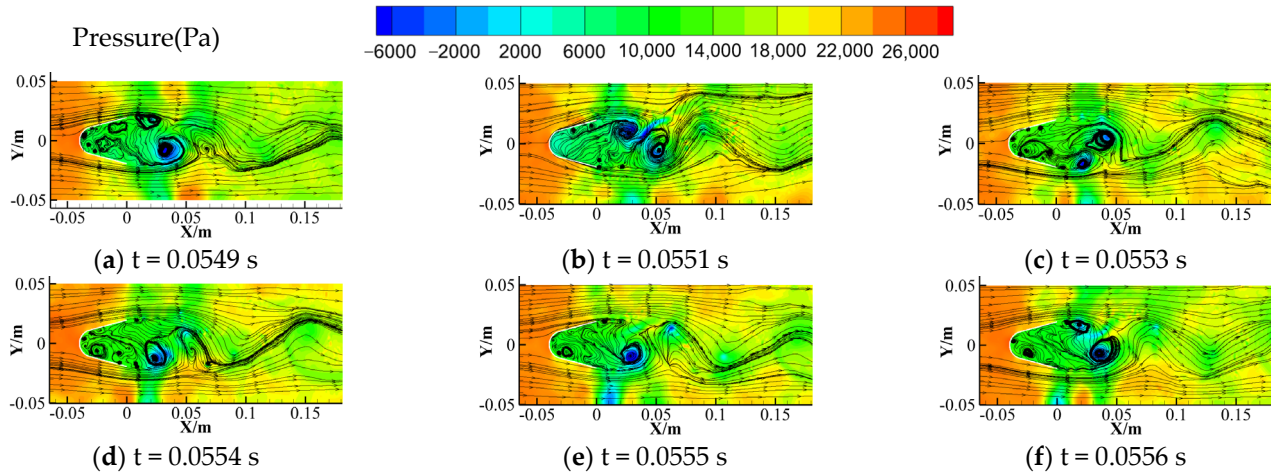
Figure 8. Temporal evolution of streamlines under X_{O2} = 23%.

Figures 9 and 10 illustrate the temporal evolution of the OH concentration and temperature fields in the central cross-section of the bluff body under X_{O2} = 23%. As shown, the alternating von Karman vortex shedding induced periodic oscillations at the flame front. Different vortex scales in the flow field affected the mixing of fuel and air. Thus, when vortex shedding progressed downstream, the surrounding unburned fresh mixture was consistently entrained by the roll-up vortex and immediately underwent combustion. Consequently, the combustion exhibited periodic exothermic pulsations owing to the generation and shedding of vortices. Furthermore, as the axial distance increased, the oscillation amplitudes of the flame in the wake increased gradually.
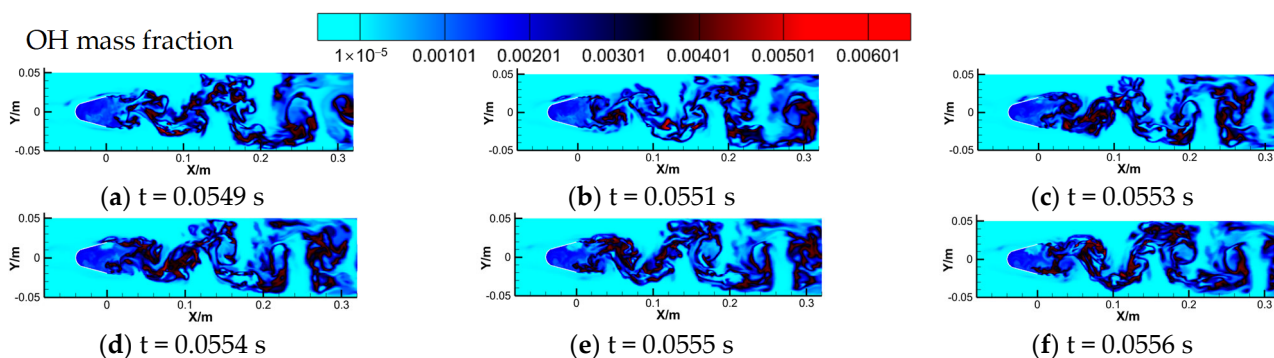

Figure 9. Temporal evolution of the OH concentration field when X_{O2} = 23%.

Figure 11 shows the temporal evolution of the streamlines in the near-wake region behind the V-shaped gutter flame holder at X_{O2} = 20.0%. In contrast to the case under X_{O2} = 23%, the vortices on both the upper and lower sides of the trailing edge of the bluff body detached simultaneously under X_{O2} = 20%, and the formed small-scale vortices progressed almost symmetrically downstream of the shear layer. In the near-wake region, numerous small-scale vortices with opposite rotational directions were symmetrically distributed on both the upper and lower sides. The reaction flow field in the shear layer was characterised by KH instability. These small-scale vortices on either side of the shear

layer strengthened as they propagated downstream. As depicted in Figure 11, the vortices situated separately in the upper and lower shear layers at almost the same axial position further developed gradually downstream. When the vortex reached a certain scale, the wake width of the reaction flow increased accordingly. However, this widening was accompanied by a stronger squeezing effect from the outer nonreactive flow. Consequently, large-scale vortices began to interact with one another, squeezed each other, and adaptively retreated to their respective optimal positions. Meanwhile, the symmetrically distributed vortex transformed progressively into a staggered arrangement. The reaction flow ultimately developed into an asymmetric and alternating vortex structure characterised by BVK instability, which resulted in substantial fluctuations in the reaction flow wake. Figure 11a–f show one complete shedding cycle, and the estimated vortex shedding period and shedding frequency were approximately 3×10^{-3} s and 333 Hz, respectively.
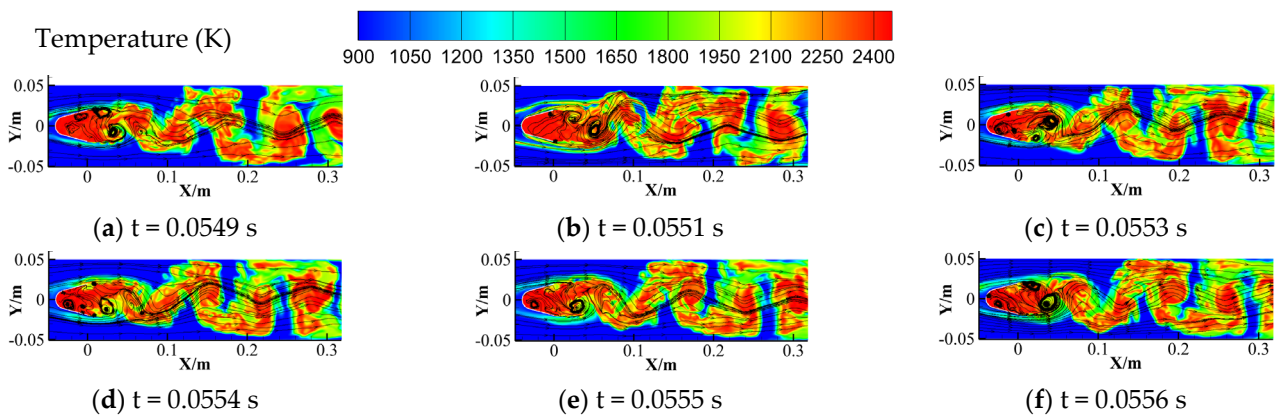

Figure 10. Temporal evolution of the temperature field when X_{O2} = 23%.
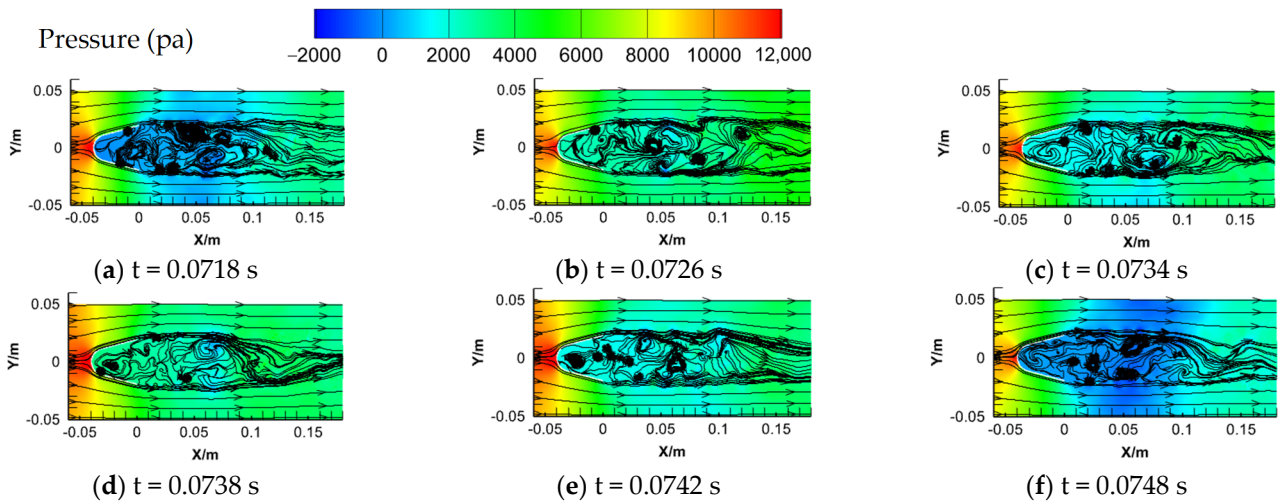

Figure 11. Temporal evolution of streamlines when X_{O2} = 20%.

The temporal evolution of the OH concentration and temperature fields in the central cross-section of the bluff body when X_{O2} = 20.0% are presented in Figures 12 and 13, respectively. Both the OH concentration and temperature in the reaction flow decreased as the oxygen mass fraction decreased from 23% to 20%. The flame behind the V-shaped gutter flame holder exhibited an almost linear behaviour with an extremely low oscillation amplitude. However, numerous high-wavelength wrinkles appeared on the flame surface, and the interface between the flame and outer nonreaction flow indicated a wavy shape, thus signifying KH instability. Santosh et al. [34] demonstrated that highly exothermic and stable flames are typically dominated by KH shear-layer instability.
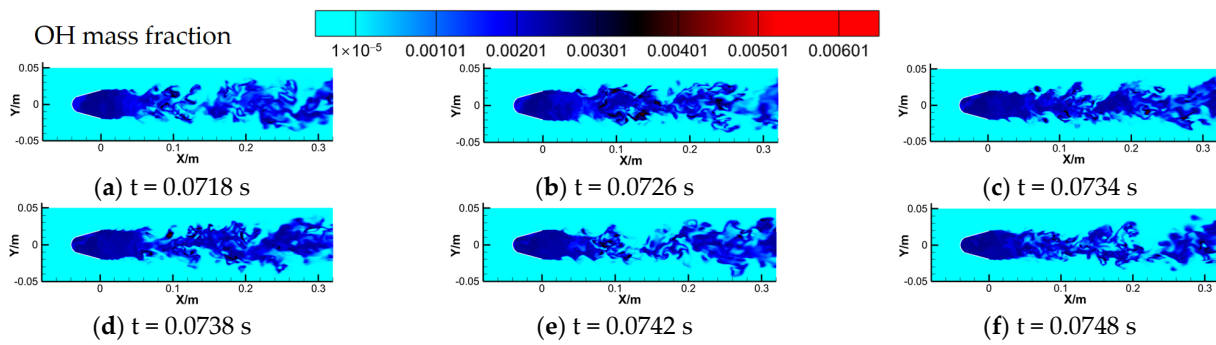
Figure 12. Temporal evolution of the OH concentration field when $X_{O2} = 20.0\%$.
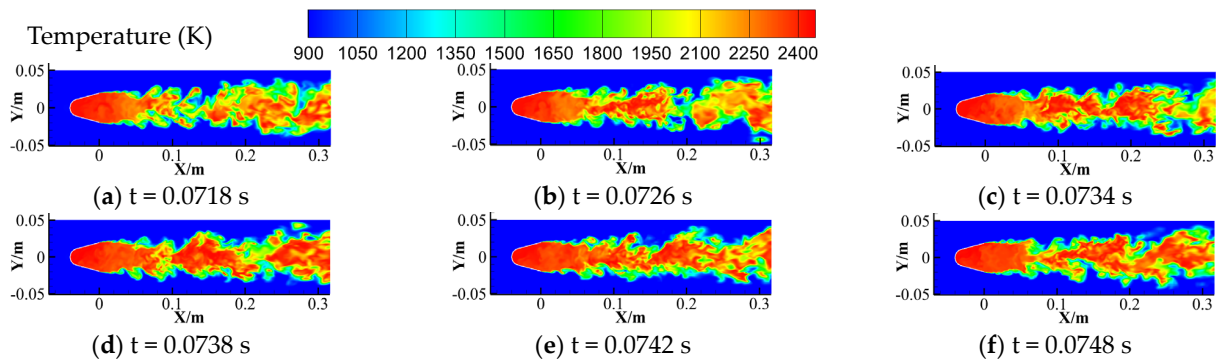

Figure 13. Temporal evolution of the temperature field when $X_{O2} = 20.0\%$.

Figure 14 shows the temporal evolution of the streamlines in the near-wake zone behind the V-shaped bluff body at $X_{O2} = 17.0\%$. The vortices on both sides of the shear layer in the trailing-edge region of the bluff body presented an approximately symmetrical distribution; however, their scales differed significantly. The vortices interacted with each other and the surrounding flow field as they progressed downstream, during which large-scale vortices developed rapidly. In contrast, the development of small-scale vortices was inhibited. Consequently, the transition from KH instability to BVK instability occurred earlier. Figure 14 illustrates the progressive evolution of the vortex in the near-wake region behind the V-shaped gutter flame holder, which included the transition from KH instability to BVK instability and ultimately caused the vortex to attenuate, fragment, and disappear. The estimated vortex-shedding period was approximately 0.0026 s, which corresponded to a shedding frequency of approximately 385 Hz.
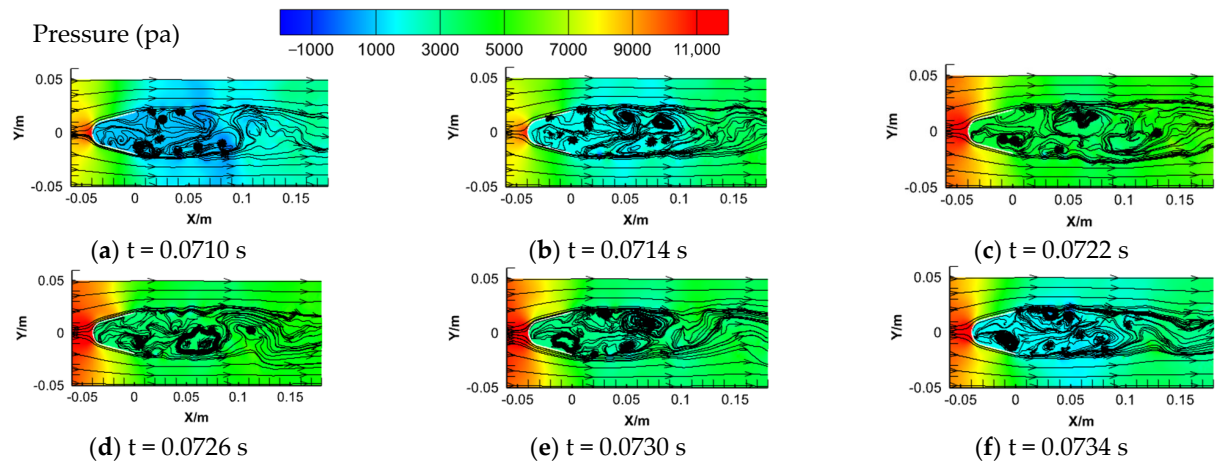

Figure 14. Temporal evolution of streamlines at $X_{O2} = 17\%$.

Figures 15 and 16 show the temporal evolution of the OH concentration and temperature fields in the central cross-section of the reaction flow under X_{O2} = 17%. As the oxygen content decreased from 20% to 17%, the OH concentration and temperature decreased significantly within the reaction flow, which corresponded to a significant decrease in both the reaction intensity and exothermic reaction. Furthermore, the flame front in the shear layer near the trailing edge zone continued to experience KH instability. In contrast, in the recirculation zones downstream, the flame front exhibited slight up–down oscillations, which is consistent with BVK instability.
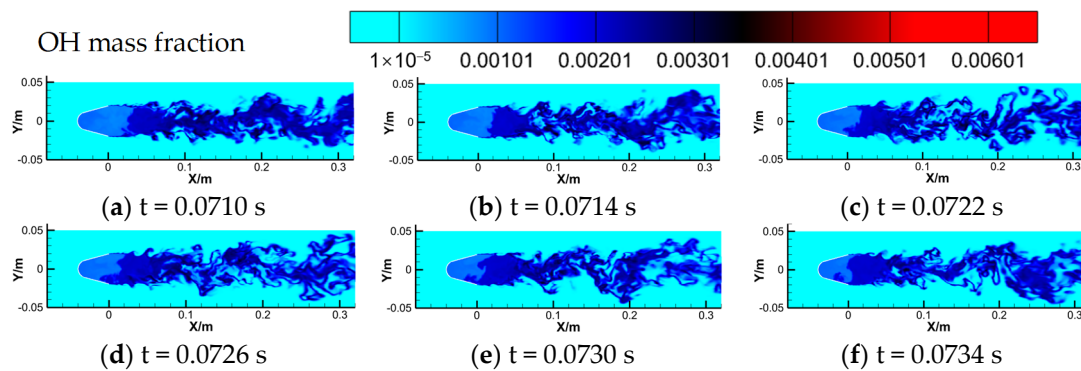

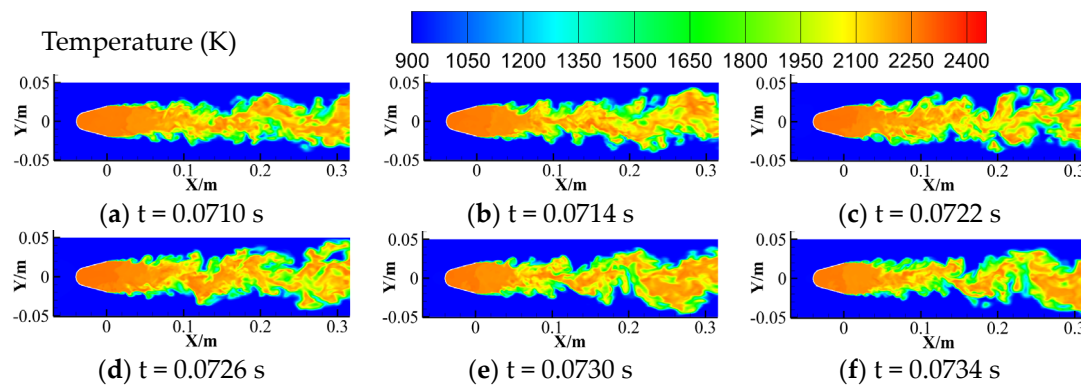**Figure 15.** Temporal evolution of the OH concentration field when X_{O2} = 17.0%.

Figure 16. Temporal evolution of the temperature field when X_{O2} = 17.0%.

Figure 17 shows the temporal evolution of the streamlines behind the V-shaped gutter flame holder at X_{O2} = 14%. As shown, the pressure difference between the recirculation zone and outer free stream was significant. The rolling up of the trailing-edge vortex behind the V-shaped gutter flame holder was extremely large, and it alternately detached from the upper and lower separated free shear layers. The wake of the V-shaped gutter flame holder experienced substantial up–down oscillations and indicated clear BVK instability with a large-scale vortex roll-up and periodic shedding. Based on the temporal evolution of the streamlines (Figure 17), the vortex-shedding period was estimated to be approximately 0.001 s, which corresponded to a vortex-shedding frequency of approximately 1000 Hz.

Figures 18 and 19 show the transient changes in the OH concentration and temperature fields at the central cross-section of the reaction flow when X_{O2} = 14%. The results showed that the flame in the combustor was almost extinguished, with only a few OH radicals appearing inside the V-shaped gutter cavity, accompanied by a fluctuating flame shape and location. Under the effect of shear forces, the flame fragments and hot flue gas periodically detached from the trailing edge of the V-shaped gutter cavity and subsequently entrained into the separated free shear layer, thus resulting in intermittent ignition and extinction processes owing to the interaction between the hot flame fragments and the nonreactive combustible mixture in the separated free shear layer. As shown in Figure 19, the high-temperature flue gas was entrained by the shed vortices, continued to propagate

downstream, and mixed with the nonreaction flow, thus resulting in a lower flue gas temperature and the gradual achievement of a uniform temperature distribution.
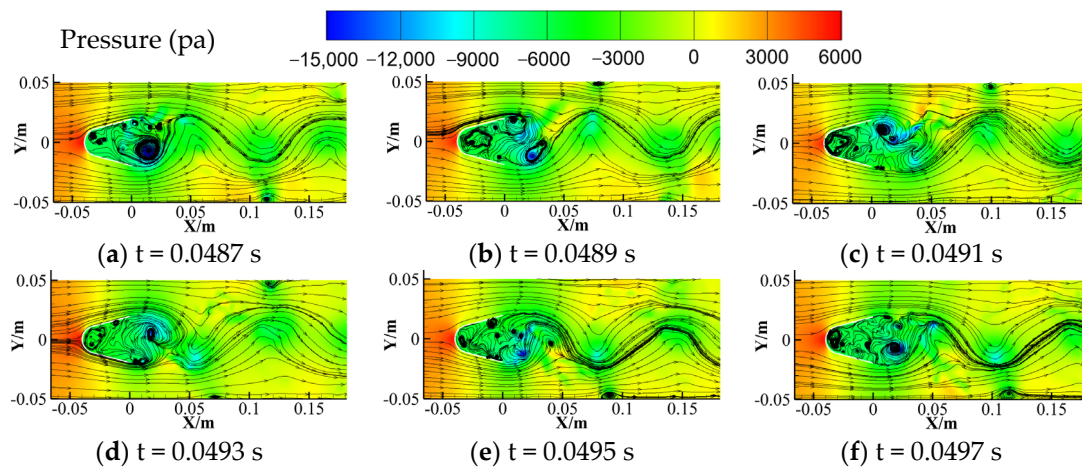

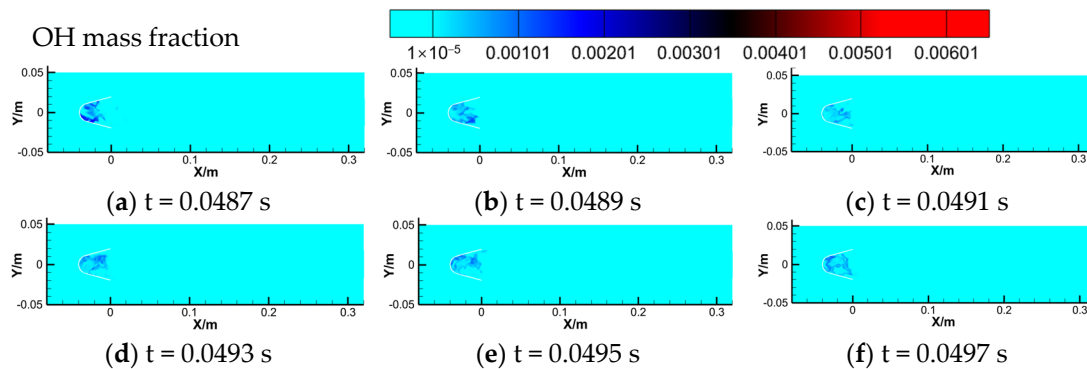**Figure 17.** Temporal evolution of streamlines when X_{O2} = 14.0%.

Figure 18. Temporal evolution of the OH concentration field when X_{O2} = 14.0%.
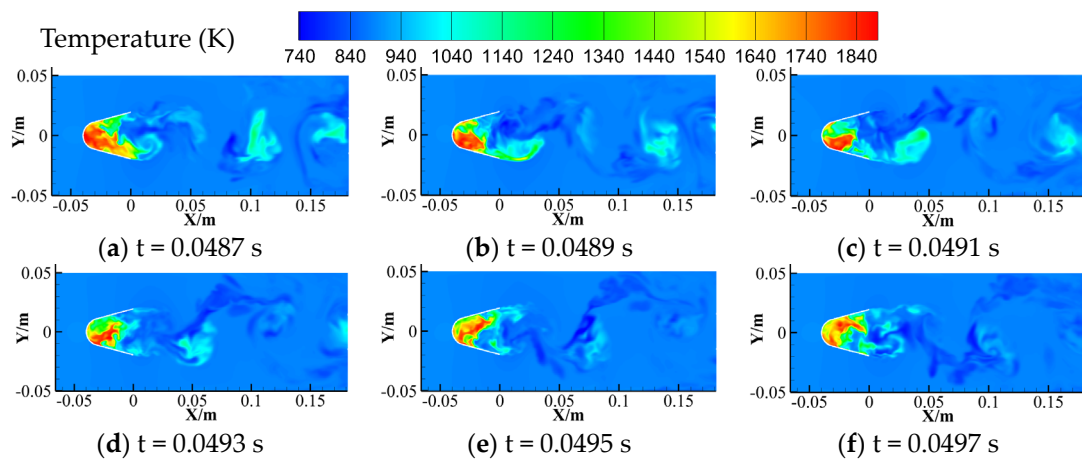

Figure 19. Temporal evolution of the temperature field when X_{O2} = 14.0%.

3.3. Spectral Analysis

As exothermic and pressure pulsation are typically utilised as indicators to monitor the dynamics of combustion [35,36], we analysed the spectrum (including the exothermic and pressure pulsations) when X_{O2} = 14–23%, T = 900–1100 K, Ma = 0.2, and p = 0.1 MPa. Seven monitoring points were arranged along the flow channel to monitor the pressure and exothermic pulsations at different oxygen contents, as illustrated in Figure 20. Monitoring

points M1 to M7 were located 2, 40, 70, 150, 200, 400, and 600 mm from the trailing edge of the bluff body, respectively. The pressure profiles recorded at T = 900 K (see Figure 21) were analysed via the fast Fourier transform, as expressed in Equation 1, to characterise the frequency variations of the measured fluctuating pressure. The total pressure pulsations observed at multiple monitoring points showed the same trend at each oxygen level. Here, the main frequency remained constant, whereas the amplitude of the pulsation varied significantly. In particular, monitoring point M2 was situated at the interface between the recirculation zone and the main stream, where a separated free shear layer existed, thus resulting in relatively high-amplitude pressure pulsations. Moreover, the separated free shear layer significantly affected the dynamic combustion characteristics [37]. Therefore, M2 was selected as the monitoring point for spectral analysis under varying oxygen contents and inflow temperatures.

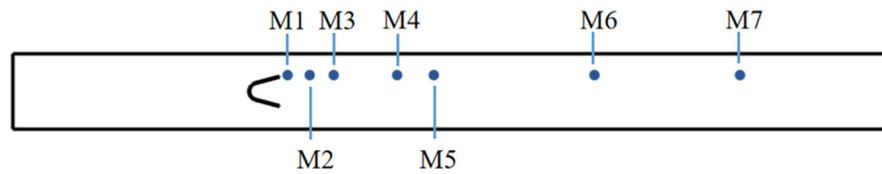$$f(x) = a_0 + \sum_{1}^{\infty}\left(a_n \cos\frac{n\pi x}{L} + b_n \sin\frac{n\pi x}{L}\right) \tag{1}$$

Figure 20. Locations of monitoring points.

(**a**) X_{O2} = 23%

(**b**) X_{O2} = 20%
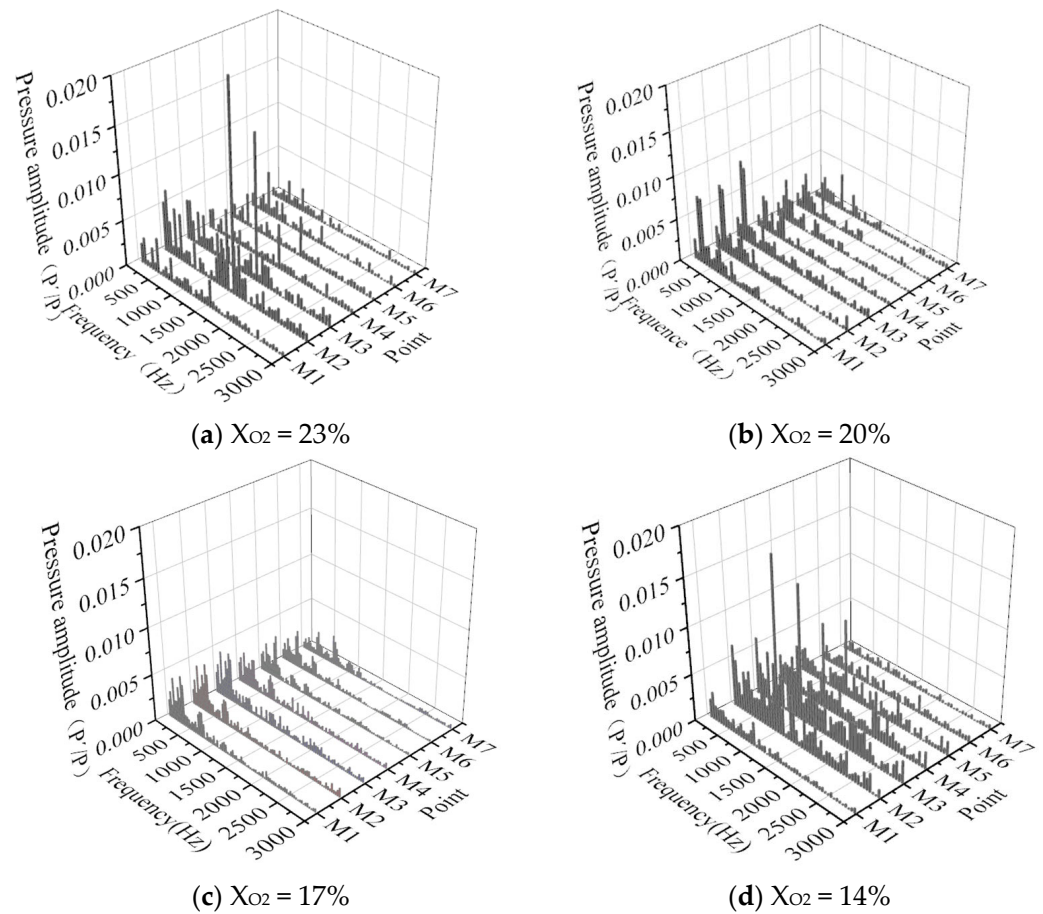
(**c**) X_{O2} = 17%

(**d**) X_{O2} = 14%

Figure 21. Frequency domain analysis of pressures measured at seven monitoring points under different oxygen contents and T = 900 K.

Figures 22 and 23 show the frequency spectra of the dynamic pressure and exothermic pulsations, respectively, recorded at monitoring point M2 over an oxygen content ranging from 23% to 14% and temperatures ranging from 900 to 1100 K. The effects of either the oxygen content or temperature on the primary frequencies and amplitudes of both pressure and exothermic pulsations within the combustion chamber were apparent. As shown in the figures, the chemically reacting flow within the separated shear layer behind the V-shaped gutter transformed between KH instability and BVK instability at different temperatures and oxygen contents. For the condition involving the entire chemically reacting flow dominated by BVK instability (including cases 1, 7, 11, and 12), the primary frequencies of both the pressure and exothermic pulsations were identical under each operational condition. Furthermore, both the pressure signals and exothermic fluctuations exhibited a well-defined narrow band in the frequency spectrum, with primary frequencies ranging from approximately 1300 to 1600 Hz. This phenomenon was caused by significant BVK oscillations within the separated shear layer, which were caused by the intense exothermic combustion and fluid hydrodynamics of the V-shaped gutter flame holder. Thus, similar primary frequencies were identified for both the pressure and exothermic pulsations, where their primary frequencies were almost identical to the frequencies associated with asymmetric periodic large-scale vortex shedding, as depicted in Figure 5. As the flame approached extinction in Case 4, the exothermic combustion decreased significantly and was accompanied by a reduction in gas expansion and alterations in viscosity. The predominant effect of exothermic reactions on the flow field originated primarily from gas expansion, baroclinic production, and viscosity alterations caused by the release of combustion heat [25]. Consequently, the effects of exothermic combustion and gas expansion on the flow field pulsations became almost negligible. The overall behaviour of the reacting flow was governed by asymmetric BVK vortex shedding induced by fluid dynamics and hydrodynamics. Notably, the primary frequency of the pressure fluctuations exhibited an extremely narrow band and prominent characteristics, featuring a main frequency of 1014 Hz. Although all reacting flows within the separated shear layers for Cases 1, 4, 7, 11, and 12 were governed by BVK instability, the primary frequency under near-extinction conditions was significantly lower than that observed in high-intensity reactive flows. This discrepancy implies that the exothermic combustion, gas expansion, and viscosity changes collectively exerted a substantial effect on the frequency of BVK instability. For the remaining conditions in which the chemically reacting flow within the separated shear layer was dominated by KH instability, as opposed to the cases dominated by BVK instability, the primary frequency of the pressure pulsations was no longer identical to that of the exothermic pulsations. Because the combustion stability dominated by KH instability was greater than that dominated by BVK instability [25], the exothermic combustion within the separated shear layer became more uniform and smooth. Consequently, the exothermic pulsations demonstrated the absence of a prominent primary frequency and instead exhibited a uniform frequency distribution across the frequency spectrum. Meanwhile, the primary frequency of the pressure pulsations remained less distinct, whereas both the primary frequency and amplitude of the pressure pulsations decreased significantly. In particular, in cases dominated by KH instability, the primary frequency ranged from 300 to 550 Hz, which was significantly lower than those observed in the cases dominated by BVK instability. This substantial alteration is attributed to the suppression of the large-scale, nonsymmetric vortex shedding structure behind the V-shaped gutter flame holder. The prominent feature of the reactive flow was governed by the significantly diminished KH instability flow fluctuations; meanwhile, the reactive flow exhibited a minor sinuous structure in the far-downstream region. This phenomenon was caused by a persistent change in combustion intensity, which altered the density variation across the flame and was consistent with the decrease in the vorticity damping term caused by flow dilatation. Consequently, the interactions between the exothermicity and shear changed significantly.
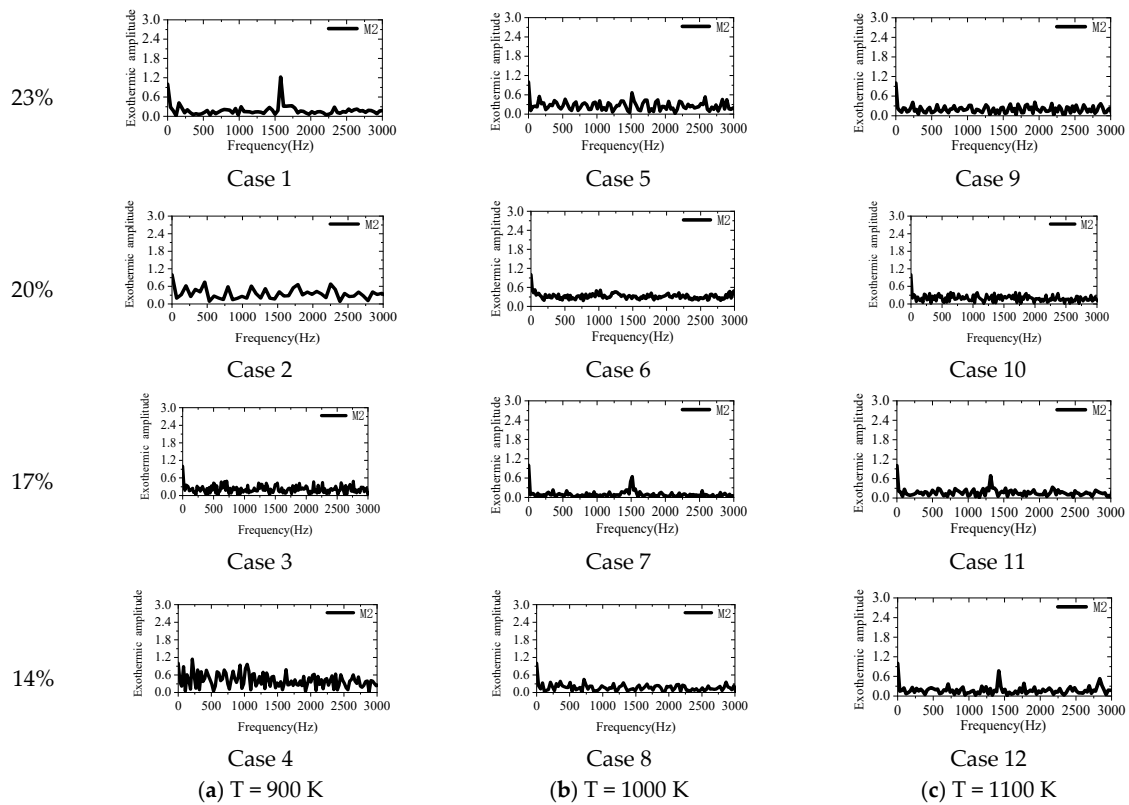
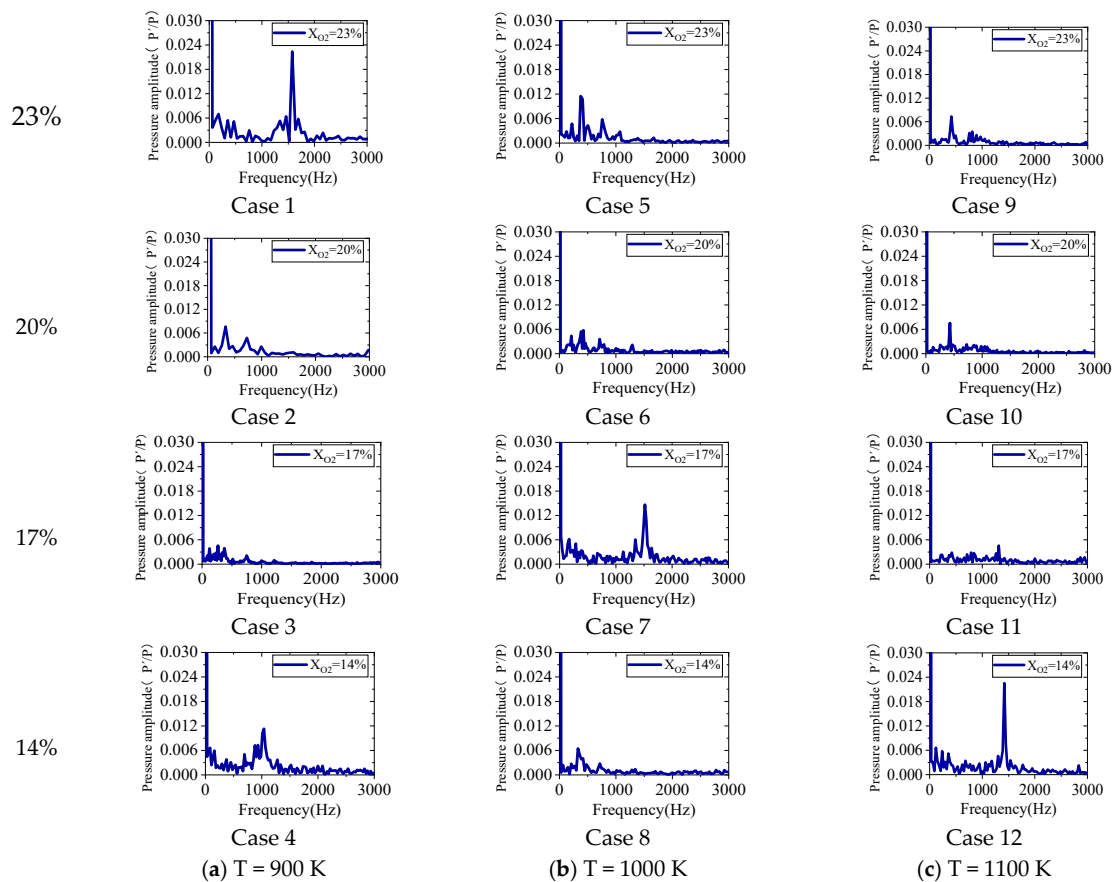**Figure 22.** Variations in exothermic pulsation with oxygen content at different inflow temperatures.

Figure 23. Variation in pressure pulsation with oxygen content at different inflow temperatures.

4. Conclusions

An LES numerical simulation was performed to investigate the dynamic combustion characteristics of V-shaped bluff-body stabilised diffusion flames, including vortex–flame interactions, vortex shedding patterns, flame morphology, exothermic pulsation, and pressure pulsation, under an oxygen mass fraction range of 14–23% and temperatures of 900–1100 K.

The results demonstrated a significant nonlinear effect of the oxygen concentration on the flame/flow behaviours downstream of the bluff-body flame holder at various temperatures. By changing the oxygen content and inflow temperature within the separated shear layer, BVK instability and KH instability transitioned between each other. Moreover, BVK instability dominated the wake flow/flame behaviour, and its oscillation amplitude changed with the oxygen content. BVK instability was suppressed by increasing the temperature at 23% and 20% oxygen content and enhanced by increasing the temperature at 17% and 14% oxygen content.

The transition from KH instability to BVK instability in the separated shear layer involved two mechanisms: (1) Symmetric small-scale vortices on both sides propagated downstream and enlarged gradually. Upon reaching a specific scale, these vortices interacted underneath and experienced enhanced compressive effects from the outer nonreactive flow, thus resulting in the transitioning of the upper and lower vortices into a staggered arrangement. (2) Symmetrical vortices with distinct scales interacted with each other downstream, thus prompting the rapid development of larger-scale vortices that compressed smaller vortices and induced BVK instability.

The results of spectral analysis revealed that during BVK instability, the pressure and exothermic pulsations exhibited coincident primary frequencies and indicated a lower primary frequency within the range of 1300 to 1600 Hz. Conversely, during KH instability, owing to the more uniform exothermic combustion, the exothermic pulsations showed few discernible primary frequencies, whereas the pressure pulsations maintained a lower frequency ranging from approximately 300 to 550 Hz.

Author Contributions: Conceptualization, F.D.; methodology, F.Z.; validation, S.Q.; investigation, M.Z.; resources, H.Z.; writing—original draft preparation, F.D.; writing—review and editing, Z.W. and Y.X.; funding acquisition, X.L. All authors have read and agreed to the published version of the manuscript.

Data Availability Statement: The data that support the findings of this study are available from the corresponding author upon reasonable request.

Conflicts of Interest: The authors declare no conflicts of interest.

References

1. Yang, M.; Tian, Y.; Guo, M.; Le, J.; Zhang, H.; Zhang, C. Optimized design of aero-engine high temperature rise combustion chamber based on "kriging-NSGA-II". *J. Braz. Soc. Mech. Sci. Eng.* **2023**, *45*, 59. [CrossRef]
2. Li, J.; Chen, J.; Jin, W.; Yuan, L.; Hu, G. The design and performance of a RP-3 fueled high temperature rise combustor based on RQL staged combustion. *Energy* **2020**, *209*, 118480. [CrossRef]
3. Zhang, R.; Huang, X.; Fan, W.; Bai, N. Influence of injection mode on the combustion characteristics of slight temperature rise combustion in gas turbine combustor with cavity. *Energy* **2019**, *179*, 603–617. [CrossRef]
4. Zhou, L.; Zhong, L.; Liu, Z.; Wei, H. Toward highly-efficient combustion of ammonia–hydrogen engine: Prechamber turbulent jet ignition. *Fuel* **2023**, *352*, 129009. [CrossRef]
5. Sun, Z.; Cui, M.; Ye, C.; Yang, S.; Li, X.; Hung, D.; Xu, M. Split injection flash boiling spray for high efficiency and low emissions in a GDI engine under lean combustion condition. *Proc. Combust. Inst.* **2021**, *38*, 5769–5779. [CrossRef]
6. Cohen, J.; Anderson, T. Experimental Investigation of Near-Blowout Instabilities in a Lean, Premixed Step Combustor. In Proceedings of the 34th Aerospace Sciences Meeting and Exhibit, Reno, NV, USA, 15–18 January 1996; p. 819.

7. Lieuwen, T.C.; Yang, V. *Combustion Instabilities in Gas Turbine Engines: Operational Experience, Fundamental Mechanisms, and Modeling*; American Institute of Aeronautics and Astronautics: Reston, VA, USA, 2005.
8. Riahi, Z.; Bounaouara, H.; Hraiech, I.; Mergheni, M.A.; Sautet, J.-C.; Nasrallah, S.B. Combustion with mixed enrichment of oxygen and hydrogen in lean regime. *Int. J. Hydrogen Energy* **2017**, *42*, 8870–8880. [CrossRef]
9. Malbois, P.; Salaün, E.; Rossow, B.; Cabot, G.; Bouheraoua, L.; Richard, S.; Renou, B.; Grisch, F. Quantitative measurements of fuel distribution and flame structure in a lean-premixed aero-engine injection system by kerosene/OH-PLIF measurements under high-pressure conditions. *Proc. Combust. Inst.* **2019**, *37*, 5215–5222. [CrossRef]
10. Weigand, P.; Meier, W.; Duan, X.R.; Stricker, W.; Aigner, M. Investigations of swirl flames in a gas turbine model combustor: I. Flow field, structures, temperature, and species distributions. *Combust. Flame* **2006**, *144*, 205–224. [CrossRef]
11. Bonciolini, G.; Ebi, D.; Doll, U.; Weilenmann, M.; Noiray, N. Effect of wall thermal inertia upon transient thermoacoustic dynamics of a swirl-stabilized flame. *Proc. Combust. Inst.* **2019**, *37*, 5351–5358. [CrossRef]
12. Vignat, G.; Durox, D.; Prieur, K.; Candel, S. An experimental study into the effect of injector pressure loss on self-sustained combustion instabilities in a swirled spray burner. *Proc. Combust. Inst.* **2019**, *37*, 5205–5213. [CrossRef]
13. Soundararajan, P.R.; Vignat, G.; Durox, D.; Renaud, A.; Candel, S. *Effect of Different Fuels on Combustion Instabilities in an Annular Combustor*; Turbo Expo: Power for Land, Sea, and Air; American Society of Mechanical Engineers: New York, NY, USA, 2020; p. V04BT04A046.
14. Gao, T.; Liang, J.; Sun, M.; Zhong, Z. Dynamic combustion characteristics in a rectangular supersonic combustor with single-side expansion. *Proc. Inst. Mech. Eng. Part G J. Aerosp. Eng.* **2017**, *231*, 1862–1872. [CrossRef]
15. Kang, J.; Sung, H.-G. Kerosene/GOx dynamic combustion characteristics in a mixing layer under supercritical conditions using the LES-FPV approach. *Fuel* **2017**, *203*, 579–590. [CrossRef]
16. Liu, C.; Zhang, J.; Yang, T.; Ma, Y. Bluff-Body Flames in Hot and Diluted Environments. In Proceedings of the ASME Power Conference, Lake Buena Vista, FL, USA, 24–28 June 2018; American Society of Mechanical Engineers: New York, NY, USA, 2018; p. V001T01A002.
17. Roy, R.N.; Sreedhara, S. A numerical study on the influence of airstream dilution and jet velocity on NO emission characteristics of CH4 and DME bluff-body flames. *Fuel* **2015**, *142*, 73–80. [CrossRef]
18. Wang, G.; Si, J.; Xu, M.; Mi, J. MILD combustion versus conventional bluff-body flame of a premixed CH4/air jet in hot coflow. *Energy* **2019**, *187*, 115934. [CrossRef]
19. Kumar, P.; Mishra, D. Characterization of bluff-body stabilized LPG jet diffusion flame with N2 dilution. *Energy Convers. Manag.* **2008**, *49*, 2698–2703. [CrossRef]
20. Mishra, D.; Kumar, P. Effects of N_2 gas on preheated laminar LPG jet diffusion flame. *Energy Convers. Manag.* **2010**, *51*, 2144–2149. [CrossRef]
21. Hosseini, S.E.; Wahid, M.A. Investigation of bluff-body micro-flameless combustion. *Energy Convers. Manag.* **2014**, *88*, 120–128. [CrossRef]
22. Noor, M.; Wandel, A.P.; Yusaf, T. Numerical study of oxygen dilution and temperature distribution of biogas combustion in Bluff-body MILD burner. In Proceedings of the 7th Australian Combustion Symposium (ACS 2013), Perth, Australia, 6–8 November 2013; University of Western Australia: Crawley, Australia, 2013; pp. 299–303.
23. Erickson, R.; Soteriou, M. The influence of reactant temperature on the dynamics of bluff body stabilized premixed flames. *Combust. Flame* **2011**, *158*, 2441–2457. [CrossRef]
24. Erickson, R.; Soteriou, M.; Mehta, P. The influence of temperature ratio on the dynamics of bluff body stabilized flames. In Proceedings of the 44th AIAA Aerospace Sciences Meeting and Exhibit, Reno, NV, USA, 9–12 January 2006; p. 753.
25. Shanbhogue, S.J.; Husain, S.; Lieuwen, T. Lean blowoff of bluff body stabilized flames: Scaling and dynamics. *Prog. Energy Combust. Sci.* **2009**, *35*, 98–120. [CrossRef]
26. Emerson, B.; O'Connor, J.; Juniper, M.; Lieuwen, T. Density ratio effects on reacting bluff-body flow field characteristics. *J. Fluid Mech.* **2012**, *706*, 219–250. [CrossRef]
27. Emerson, B.; Lundrigan, J.; O'Connor, J.; Noble, D.; Lieuwen, T. Dependence of the bluff body wake structure on flame temperature ratio. In Proceedings of the 49th AIAA Aerospace Sciences Meeting including the New Horizons Forum and Aerospace Exposition, Orlando, FL, USA, 4–7 January 2011; p. 597.
28. Wang, B.-C.; Bergstrom, D.J. A dynamic nonlinear subgrid-scale stress model. *Phys. Fluids* **2005**, *17*, 035109. [CrossRef]
29. Xu, L.; Zhang, Y.; Tang, Q.; Johansson, B.; Yao, M.; Bai, X.-S. LES/FGM investigation of ignition and flame structure in a gasoline partially premixed combustion engine. *Proc. Combust. Inst.* **2023**, *39*, 4851–4860. [CrossRef]
30. Kundu, K.; Penko, P.; VanOverbeke, T. A practical kinetic mechanism for computing combustion in gas turbine engines. In Proceedings of the 35th Joint Propulsion Conference and Exhibit, Los Angeles, CA, USA, 20–24 June 1999; p. 2218.
31. Roach, J.; Fisher, T.; Frankel, S.; Sekar, B.; Kiel, B. Cfd predictions of damköhler number fields for reduced order modeling of v-gutter flame stability. In Proceedings of the 46th AIAA Aerospace Sciences Meeting and Exhibit, Reno, NV, USA, 7–10 January 2008; p. 509.
32. Liu, X. Study on Low Emission Combustion Chamber Design and Premixed Combustion Characteristics. Ph.D. Thesis, Harbin Engineering University, Harbin, China, 2017.
33. Wu, H.; Ma, P.C.; Lv, Y.; Ihme, M. MVP-Workshop Contribution: Modeling of Volvo bluff body flame experiment. In Proceedings of the 55th AIAA Aerospace Sciences Meeting, Grapevine, TX, USA, 9–13 January 2017; p. 1573.

34. Santosh Kumar, T.; Alemela, P.; Kok, J.B. Dynamics of Flame Stabilized by Triangular Bluff Body in Partially Premixed Methane-Air Combustion. In *Turbo Expo: Power for Land, Sea, and Air*; American Society of Mechanical Engineers: New York, NY, USA, 2011; pp. 1017–1026.

35. Putnam, A.A.; Dennis, W.R. Organ-pipe oscillations in a flame-filled tube. *Symp. (Int.) Combust.* **1953**, *4*, 566–575. [CrossRef]

36. Zinn, B.T.; Powell, E.A. Nonlinear combustion instability in liquid-propellant rocket engines. *Symp. (Int.) Combust.* **1971**, *13*, 491–503. [CrossRef]

37. Schadow, K.; Gutmark, E. Combustion instability related to vortex shedding in dump combustors and their passive control. *Prog. Energy Combust. Sci.* **1992**, *18*, 117–132. [CrossRef]